

SALOS - a UWB Single Anchor Localization System based on CIR-vectors - Design and Evaluation

Sven Ole Schmidt¹, Marco Cimdins¹ and Horst Hellbrück¹

¹Technische Hochschule Lübeck - University of Applied Sciences, Mönkhofer Weg 239, 23562 Lübeck, Germany

Abstract

Single anchor localization systems with radio-frequency (RF) signals provide a position estimation for indoor environments and have unique challenges. For such a position estimation, angle and distance measurements are required. Whereas distance measurements are a standard in RF localization systems, angular measurements require either multi-antenna systems or selective shadowing with mechanical rotation, which is complex and costly. Another approach for resolving the ambiguity of pure distance measurements is the use of multipath propagation when the location of the anchor and the geometry of the indoor environment is given. Multipath information is available by channel impulse response (CIR) measurements. The concept of CIR-vectors for position characterization is already introduced but is not yet evaluated in real systems. A comparison of similarity metrics has not been investigated for a setup with off-the-shelf hardware. We introduce our system SALOS, a localization approach to convert real measurements into CIR-vectors and provide similarity metrics for comparison. We introduce a standard ℓ_1 -norm, advanced ℓ_1 -norm, and ℓ_1 -norm based on the sliding window. We perform 3-dimensional measurements with Qorvo's DW1000 RF chip in a grid. To increase the resolution distinct transmission bands are assembled. We modeled the expected results of the CIR-vectors based on an optimal anchor positioning and designed several similarity metrics. We evaluate the resulting position estimation. In the best case, SALOS estimates 70% of correct positions for the sliding window ℓ_1 -norm. For this case, the assessment of ambiguity, our proposed metric to quantify the demand for external information, of 0.89 is reached.

Keywords

single anchor localization, channel impulse response, effective length of CIRs, optimal anchor positioning, UWB measurements, DW1000, CIR-vector

1. Introduction

In the last ten years radio-frequency (RF)-based indoor localization complements the well-established satellite localization we all use for outdoor navigation. Successful and robust RF indoor localization started with multiple anchors. Many products recommend at least four anchors placed at each corner of a room to perform distance measurements and multilateration algorithms. If the room is large, cells of four anchors are formed to cover larger areas. Hence,

IPIN 2022 WiP Proceedings, September 5 - 7, 2022, Beijing, China

✉ sven.ole.schmidt@th-luebeck.de (S. O. Schmidt); marco.cimdins@th-luebeck.de (M. Cimdins);

horst.hellbrueck@th-luebeck.de (H. Hellbrück)


🌐 <https://www.th-luebeck.de/en/cosa/team/sven-ole-schmidt/> (S. O. Schmidt);

<https://www.th-luebeck.de/en/cosa/team/marco-cimdins/> (M. Cimdins);

<https://www.th-luebeck.de/en/cosa/team/horst-hellbrueck/> (H. Hellbrück)

🆔 0000-0001-7653-1463 (S. O. Schmidt); 0000-0002-0114-5661 (M. Cimdins); 0000-0001-7619-8015 (H. Hellbrück)

© 2022 Copyright for this paper by its authors. Use permitted under Creative Commons License Attribution 4.0 International (CC BY 4.0).

 CEUR Workshop Proceedings (CEUR-WS.org)

these systems require a large number of anchors and each anchor increases the costs for hardware, deployment, and maintenance. E.g. 50 Ultra-Wideband (UWB) anchors are deployed to cover a production facility of 1500 m² in [1].

In the recent past, single anchor localization systems became a cost-effective alternative. However, such systems for indoor environments have unique challenges. For position estimation, pure distance measurements are not enough. Additionally, angular measurements are required that need either multi-antenna systems or selective shadowing with mechanical rotation.

Technologies such as Bluetooth Low Energy (BLE) introduced angle-of-arrival in version 5.1. Together with distance measurements, single anchor localization will receive more attention [2, 3]. Grosswindhager et al. present a UWB single anchor localization system in [4]. They deploy multiple directional antennas to overcome ambiguities in the position estimation since one single antenna could not avoid a suboptimal anchor position leading to a set of position estimations instead of on fixed estimation without further processing. In [5], Wang et al. equip a single UWB anchor with an antenna array and localize tags with the distance extracted from time-of-flight measurements and the angle-of-arrival extracted from the antenna array. Cao et al. combined speed estimations extracted from UWB range with an inertial-measurement-unit to track tags that are attached to a moving robot [6]. However, angular measurements are complex and costly compared to an anchor that performs only distance measurements but are more effective than multiple anchors.

An alternative approach for resolving the ambiguity of pure distance measurements is the use of multipath propagation, exploiting the concept of virtual anchors due to reflections at walls [7]. This requires knowledge of the location of an anchor and the geometry of the indoor environment. In [8] Miao et al. discussed the optimal anchor positioning for single-hop localization systems. For a multipath-based localization system, anchor positioning is very important. We proposed to convert the given multipath components (MPC) into an overall channel impulse response (CIR) vector to determine the optimal position of the anchor via simulation [9]. Multipath information is available by CIR measurements with commercial off-the-shelf (COTS) anchors based on UWB signals. Furthermore, we have shown that assembling several UWB channels increases the bandwidth of the UWB signals and thereby the resolution [10].

In this paper, we investigate *SALOS*, a single anchor localization system, and perform measurements in a realistic setup with COTS hardware. We model MPCs via raytracing and model CIRs that we compare with real taken CIR measurements. MPC detection is ambitious, therefore this paper is also about extracting MPCs from the measured UWB CIR. For efficiency and to create a similarity metric, we convert these CIR measurements into so-called CIR-vectors. In this work, we show that the previous set assumptions are valid for measurements that are recorded by a COTS available low-cost UWB transceiver: the Qorvo DW1000. For this proof-of-concept for *SALOS*, we focus on a localization area with a single anchor node. This procedure enables the evaluation of the concept at all and is covering a minimalized-hardware approach, which is one of the main arguments for usage of single-anchor localization.

In summary, our contributions are:

- We introduce *SALOS*, a single anchor localization system based on CIR-vectors.
- We derive a CIR-vector representation of CIR measurements of Qorvo's Decawave

DW1000 RF chip with a new estimation algorithm for MPCs.

- We assemble DW1000's CIR measurements of distinct transmission bands to improve the accuracy of the MPC detection algorithm.
- We introduce two advanced similarity metrics for the comparison of CIR-vectors that consider typical measurement inaccuracies and evaluate the system performance.

The rest of the paper is organized as follows: Section 2 introduces theoretical basics for SALOS: a multipath model, a conversion from CIRs to CIR-vectors, as well as optimal anchor positioning, and a new similarity metric. Section 3 describes the processing of the CIR measurements as well as the MPC detection algorithm. The evaluation of our deployment is given in Section 4. Section 5 finally concludes the paper and provides directions for future work.

2. SALOS System Background and Components

In this section, we introduce the theoretical background for SALOS, our single anchor localization system based on CIR-vectors. First, we focus on the derivation of multipath components (MPC) based on a 3-dimensional multipath environment and form the overall channel impulse response (CIR) $h(t)$. Afterward, we show how to convert $h(t)$ into the corresponding CIR-vector \mathbf{h} . Then, we determine the optimal anchor position based on the effective length of CIRs l_e , as introduced in our previous work [9]. Finally, we will introduce three similarity metrics applied for position estimation in our localization system.

2.1. Modeling 3-dimensional Multipath Propagation

We assume that the electromagnetic signal $x(t)$ propagates from a sensor node of unknown position P_T (e.g. a *tag*) to a node of known position P_A (e.g. an *anchor*). The anchor An does not only receive the *Tag*'s signal $x(t)$ via the direct *Line-of-Sight*-path (LOS) with path length d_0 and transmission delay $\tau_0 = d_0/c_0$, with speed of light $c_0 \approx 3 \cdot 10^8$ m/s. In addition, signal echoes e.g. reflected from surfaces such as walls or objects will reach the anchor as well. Figure 1 shows an exemplary multipath environment including echo paths (depicted in blue).

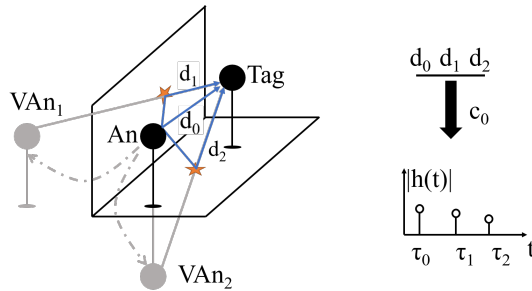


Figure 1: 3-dimensional multipath environment including one wall and the ground.

Signal echoes passing the i -th echo path result in a higher transmission delay $\tau_i > \tau_0$ since the path length of the transmission $d_i > d_0$ is longer than the LOS. To calculate the path length

of the single echo paths, we introduce the concept of *virtual anchors*. These virtual anchors (VAn) are projections of an anchor An , mirrored at the reflection surface. Figure 1 depicts them in gray. While the path length between one VAn and Tag is identical to the echo path's length d_i , the intersection between these pseudo-direct connections and the corresponding surface indicates the reflection point at the surface (in Figure 1 marked with an orange star).

Each echo path has individual effects on the transmitted signal $x(t)$, e.g. transmission delay or received power. In the following, the transmission delay τ_i in combination with the received signal amplitude a_i characterizes the *multipath component* (MPC) of the i -th echo path. Note, that the received signal amplitude a_i is decreasing with increasing path length d_i due to the path losses. The channel impulse response (CIR) $h(t)$ is the sum of the effect of all I MPCs on the transmitted signal $x(t)$ leading to the received signal $y(t)$ with:

$$y(t) = x(t) * h(t), \text{ with } h(t) = \sum_{i=0}^{I-1} a_i \cdot \delta(t - \tau_i), \quad (1)$$

where $\delta(t - \tau_i)$ is Dirac's pulse at time $t = \tau_i$.

Since the anchor's position P_A and the environment (e.g. extracted by a floor plan) are known, the CIR characterizes the corresponding tag's position P_T and enables localization systems based on a single anchor node. The optimal approach to avoid external information for these systems is to assure that the mapping from the tag position P_T to the corresponding CIR $h_{P_T}(t)$ is *bijective*. So, both a tag position is leading to a specific CIR, and the CIR is only indicating exactly this tag position. If the mapping is not designed bijectively, at least one CIR could result from two different tag positions. Therefore, external information coming from e.g. the prior position or angular measurements are required for successful localization. This assumption leads to the optimal anchor position of the localization system covered in Section 2.3.

2.2. Conversion of Channel Impulse Responses to CIR-vectors

In this section, we briefly summarize the conversion of CIRs into their corresponding vectors. By converting the continuous CIRs $h(t)$ to discrete finite vectors \mathbf{h} , we shorten the data set and enable direct quantitative comparison of the CIR-vectors. Even though we discard additional information, the remain information covered in the CIR-vectors is enough to ensure an unambiguous characterization of tag positions with the corresponding CIR-vectors [9].

Assume a fixed anchor in a given three-dimensional multipath environment. So, the unknown tag position P_T is characterized based on the received signal $y(t)$. Therefore, the underlying multipath propagation needs to be comparable, even with real measurement inaccuracies. For this purpose, the CIR $h_{P_T}(t)$ at arbitrary tag's position P_T is converted into a CIR-vector \mathbf{h}_{P_T} .

Figure 2 shows a conversion from $h_{P_T}(t)$ to \mathbf{h}_{P_T} . First, we define a bin width Δ_{bin} as a fixed time interval and split the time axis into $N \lceil \tau_{I-1} / \Delta_{bin} \rceil$ bins, where τ_{I-1} is longest transmission delay of all echo paths. Now, we check the transmission delay τ_i for each MPC to match the n -th bin and increment the corresponding entry in $\mathbf{h}_{P_T}[n]$ by one (see Algorithm 1).

For detailed information, we refer to previous work [9]. After the introduction of the CIR-vector representation, we will focus on the optimal anchor position of our localization system.

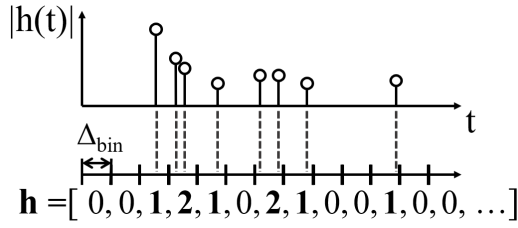


Figure 2: Conversion of CIR $h_{P_T}(t)$ to CIR-vector \mathbf{h}_{P_T} .

Algorithm 1: Conversion of CIR $h_P(t)$ consisting of I MPCs to CIR-vector \mathbf{h}_P .

Data:

Assume $\tau_{I-1} \geq \tau_i, \forall i \in \{0, \dots, I-1\}$; $N = \lceil \tau_{I-1} / \Delta_{bin} \rceil$; $\mathbf{h}_P^{(1 \times N)} = [0, 0, \dots, 0]$;

```

1 for  $i = 0, \dots, I-1$  do
2    $n = \lceil \tau_i / \Delta_{bin} \rceil$ ;
3    $\mathbf{h}_P[n] = \mathbf{h}_P[n] + 1$ ;
4 end

```

2.3. Calculation of the Effective Length of CIRs and Optimal Anchor Positioning

The optimal anchor positioning of our localization system focuses on the idea of *bijective mapping*, following an unambiguous correspondence of tag position P_T and its CIR-vector \mathbf{h}_{P_T} (derived from the CIR $h_{P_T}(t)$). To fulfill the condition of a bijective mapping, we require that the CIR-vectors of all tag positions differ from each other. Since the multipath environment is fixed and the tag position P_T is unknown, the only way to influence the CIR-vectors is by the positioning of the anchor. To evaluate the bijectivity characteristics of an anchor position in a multipath environment, we introduced in our previous work the *effective length of CIRs* l_e [9].

Next, we describe how we identify bijective mapping and we find the optimal anchor position based on the results of the comparison of the CIR-vectors. Bijectivity is given, when CIR-vectors of all tag positions are distinct. Since the MPC's amplitude, a_i is decreasing for increasing path length, we focus on the most powerful signal echoes for distinction. So we start with comparing the CIR-vectors $\mathbf{h}[n]$ at $n = 0$ with increasing n in each iteration.

Figure 3 depicts an exemplary comparison of three different CIR-vectors $\mathbf{h}_1, \mathbf{h}_2, \mathbf{h}_3$, at tag's position $\{P_{T,1}, P_{T,2}, P_{T,3}\}$ as well as the resulting effective length l_e . In the first iteration, the first bin of length Δ_{bin} of all CIR-vectors is compared with each other. Since \mathbf{h}_2 and \mathbf{h}_3 both have a [0] entered in this bin, they are indistinguishable based only on the first bin, leading to an ambiguous representation with respect to the first bin. Only \mathbf{h}_1 has a '1' noted in the first bin. Thus, \mathbf{h}_1 is already unambiguous. When a measured CIR-vector with a [1] in the first bin appears, it points back to \mathbf{h}_1 and thus to the tag position $P_{T,1}$. Since there are at least two tag positions, which do not differ with respect to the first bin, the combination of the first and the second bin are of interest. Again, \mathbf{h}_2 and \mathbf{h}_3 include the same combination with [0,1]

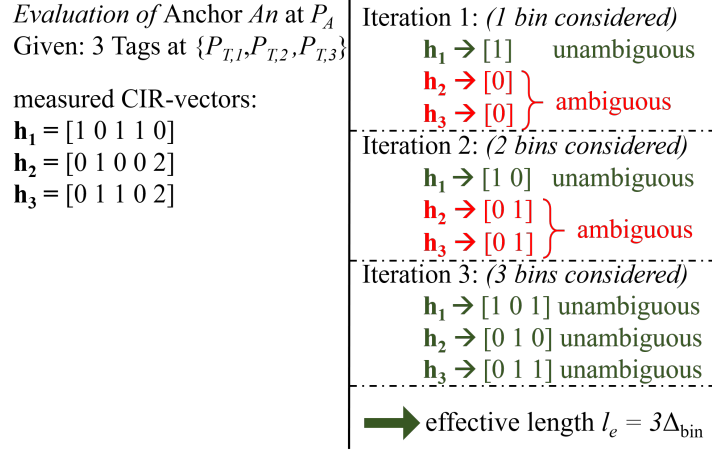


Figure 3: Comparison of CIR-vectors $\mathbf{h}_1, \mathbf{h}_2, \mathbf{h}_3$ the resulting effective length of the CIRs is $l_e = 3\Delta_{bin}$.

and are not yet distinguishable. Therefore, the next iteration including the combination of the first three bin entries is taken into account. While \mathbf{h}_2 results in $[0,1,0]$, \mathbf{h}_3 finally differs with the entries $[0,1,1]$. So, this is the first selection that all three tag positions result in distinct CIR-vectors. Following the example, not more than three bins are needed for unambiguous characterization. Since three bins are required to enable bijective mapping at the given anchor position, the smallest length of the CIR-vector to consider is $l_e = 3\Delta_{bin}$, which is the so-called *effective length of CIRs* of this anchor position. Taking more bins into account would not add any further information, but only redundancy.

Different anchor positions result in different effective lengths l_e for the same set of tag positions [9]. Therefore, anchor positions must provide unambiguous CIR-vectors for a given set of tag positions ($l_e < \infty$) to avoid the need for external information. The smaller l_e for different anchors, the more preferable is the anchor position. The anchor position with the smallest l_e is defined to be the *optimal anchor position*.

After determining the optimal anchor position, the localization system finally requires a similarity metric for accurate position estimation based on the measured CIR-vectors.

2.4. Similarity Metric for CIR-vectors

We base SALOS on a set of modeled CIR-vectors $\{\mathbf{h}_{mod}\}$, which are general constructed as described in Section 2.2. For position estimation with respect to a measured CIR-vector \mathbf{h}_{meas} (also formed as described in Section 2.2), the corresponding similarity metric needs to take measurement inaccuracies into account following from deviating positioning of the anchor or rough and bumpy reflection surfaces.

In this work, we compare the result of three different similarity metrics for the comparison of vectors. These metrics are chosen as examples because they can handle the basic idea of vector comparison with possible error-ridden bin content. In the following, the metrics' input is the general vectors \mathbf{h}_1 and \mathbf{h}_2 with the same number of entry bins N .

Assume the comparison of N bins of the vector \mathbf{h}_1 and the vector \mathbf{h}_2 . It is useful to focus on the difference between the vectors bin by bin. So, the ℓ_1 -norm is selected as the first metric.

The ℓ_1 -norm is defined as:

$$d_{\ell_1}(\mathbf{h}_1, \mathbf{h}_2) = \sum_{n=0}^{N-1} |\mathbf{h}_1[n] - \mathbf{h}_2[n]|. \quad (2)$$

In SALOS, measurement inaccuracies lead to alteration of the MPC's transmission delays τ . In the worst case, the altered delay τ is allocated to a different bin than expected during CIR-vector conversion. So, even if the corresponding MPC is estimated accurately, the measured CIR-vector differs. Therefore, we introduce our *advanced* ℓ_1 -norm $d_{ad\ell_1}(\mathbf{h}_1, \mathbf{h}_2)$, which focuses on the neighboring bins.

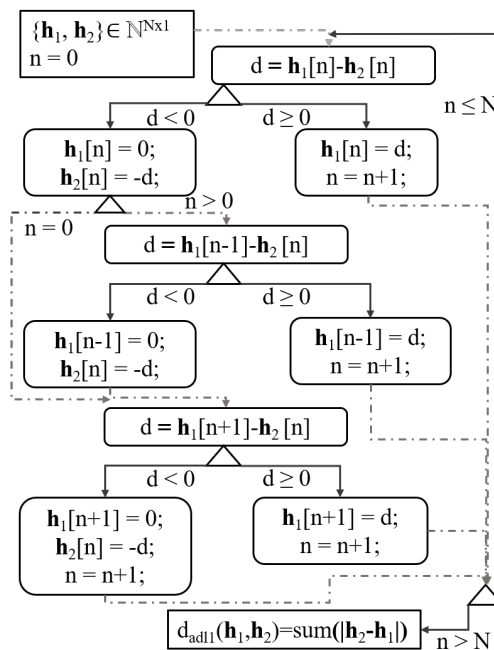


Figure 4: Block diagram of the self-developed *advanced* ℓ_1 -norm $d_{ad\ell_1}(\mathbf{h}_1, \mathbf{h}_2)$.

Figure 4 shows the algorithm as a block diagram. As with d_{ℓ_1} , the n -th bin of \mathbf{h}_1 and \mathbf{h}_2 are subtracted. When all entries of the measured CIR-vector's n -th bin $\mathbf{h}_1[n]$ are also contained in the modeled CIR-vector's n -th bin $\mathbf{h}_2[n]$, the algorithm increases the considered bin to $n = n + 1$. If not, subsequently, the previous and then the following bin of $\mathbf{h}_2[n]$ are taken into account. Note, that for $n = 0$ no previous bin exists, therefore we go directly to the following bin. In the end, the advanced ℓ_1 -norm $d_{ad\ell_1}(\mathbf{h}_1, \mathbf{h}_2)$ is the sum of the not-found CIR-vector entries of \mathbf{h}_1 .

Additionally, a third algorithm is added, which is based on the *sliding window* concept in combination with the ℓ_1 -norm. Algorithm 2 depicts the operation method of the resulting similarity metric $d_{sw}(\mathbf{h}_1, \mathbf{h}_2)$:

Algorithm 2: Similarity metric $d_{sw}(\mathbf{h}_1, \mathbf{h}_2)$.

Data:
 $\{\mathbf{h}_1, \mathbf{h}_2\} \in \mathbb{N}^{N \times 1}$; window size: $n_{sW} = 3$;
1 for $n = 0, \dots, N - n_{sW}$ **do**
2 | $d[n] = |\sum_n^{n+n_{sW}} \mathbf{h}_1[n]| - |\sum_n^{n+n_{sW}} \mathbf{h}_2[n]|$;
3 end
4 $d_{sW}(\mathbf{h}_1, \mathbf{h}_2) = \sum_{n=0}^{N-n_{sW}} |d[n]|$;

Here, to catch position estimation errors coming from measurement inaccuracies, we add up the entries of $n_{sW} = 3$ bins for both \mathbf{h}_{meas} and \mathbf{h}_{mod} and subtract them from each other. Subsequently, we shift the consideration window by one bin and add up two of the already considered bins with the next following entry.

In this section, we summarized the CIR-vector representation to characterize tag positions based on the multipath propagation of the transmit signal $x(t)$ and the resulting optimal anchor positioning for our proposed localization system. Furthermore, we presented the algorithms applied as a similarity metric for the localization system. In the next section, we will focus on the extraction of MPCs and CIR-vectors from real UWB measurements with Qorvo's Decawave DW1000 RF chip.

3. CIR-vector Estimation for UWB Measurements

After proposing the concept of SALOS, we show in this section how to assemble real UWB measurements recorded with Qorvo's DW1000 RF chip and the conversion to real CIR-vectors. The assemblage of multiple transmit signals on distinct transmission bands increases the effective bandwidth of the system without hardware change.

3.1. Signal Processing and Assemblage of Decawave DW1000 UWB Measurements

The COTS available DW1000 RF chip provides distance estimation between tag and anchor via *two-way-ranging* (TWR). In addition, it records the received signals at predefined transmission channels. In the following, we will focus on the transmission parameters listed in Table 1:

For details regarding the TWR of the DW1000 we refer to [11]. Note: following [12], we extract the corresponding received signal of DW1000's registers in the *Final*-message of the TWR. This results in a distance estimation, which is directly correlated to the received signal recorded by the DW1000 system.

In our previous work [10], we showed that the assemblage of received signals of multiple transmissions on distinct transmission bands equals the received signal for one simultaneous transmission at all these transmission bands.

In order to apply this method for the DW1000, we apply pre-processing that is proposed in previous work [13].

The receive signal consists of \hat{K} integer-valued I/Q-samples $y_{raw}[kT_S]$ with sampling time $T_S \approx 1 \text{ ns} = 1/(2B)$ resulting from bandwidth $B \approx 500 \text{ MHz}$ for each UWB channel. The

Table 1

Parameters for the DW1000 UWB measurements.

DW1000 parameter	value
UWB transmission band channel 1 $B_{T,1}$	[3.25, 3.75] GHz
UWB transmission band channel 2 $B_{T,2}$	[3.75, 4.25] GHz
UWB transmission band channel 3 $B_{T,3}$	[4.25, 4.75] GHz
pulse repetition frequency	64 MHz
preamble length	128
preamble acquisition chunk size	8
Tx and Rx preamble code	9
data rate	6.8 MBit/s

recorded $Rmarker$ indicates the beginning of the received signal in the K' -sized sample set. The received signal starts with the sample indicated by the $Rmarker$, therefore, a total of K samples of the received signal are available leading to $y_{raw}[kT_S]$, $k = 0, \dots, K - 1$.

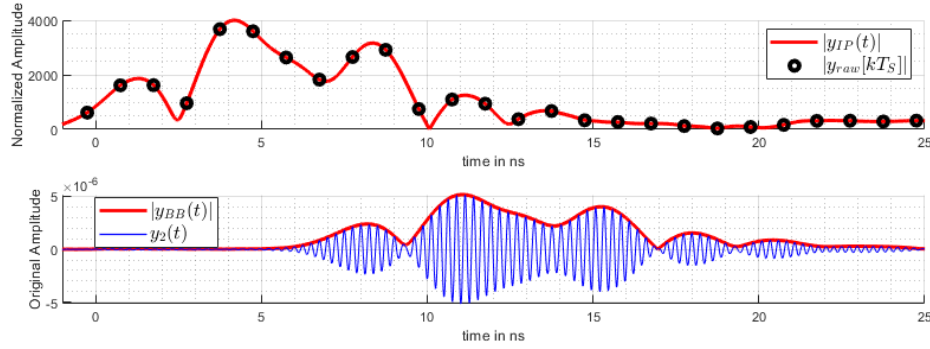
**Figure 5:** Pre-processing of the DW1000 Received Signals.

Figure 5 depicts the magnitude of an exemplary raw received signal $|y_{raw}[kT_S]|$ in the baseband at center frequency $f_c = 0$, with bandwidth B (sampled signal shown with black dots). We interpolate all K samples by convolution with a sinc-function with zero-crossings of distance $T_{sinc} = 1/(2B) = T_S$ [13]. This fulfills the Nyquist-Shannon sampling criterion. The resulting interpolated signal $y_{IP}(t)$ is shown in Figure 5 (red line)

$$y_{IP}(t) = \sum_{k=0}^{K-1} y_{raw}[kT_S] \cdot \frac{\sin(\pi \cdot t/T_S)}{\pi \cdot t/T_S} \cdot \delta(t - kT_S). \quad (3)$$

The DW1000 also provides the power A_{RX} of the received signal to reconstruct the real received amplitude of the received signal simply by multiplying the signal. Also, a phase offset ϕ_0 is included in every measurement. This offset is extracted by setting the phase at a self-defined time-stamp T_0 to zero. Additionally, the signal is time-shifted by τ_0 to include the TWR distance estimation d_0 and align the signal echo in time. As we record M measurements

with the identical setup at the same position, we are able to average these measurements after normalization with A_{RX} and phase correction by $\varphi_0(T_0)$ to determine $y_{BB}(t)$:

$$y_{BB}(t) = \sum_{m=0}^{M-1} y_{IP}^m(t - \tau_0) \cdot \sqrt{10^{(A_{RX}^m/10)}} \cdot \exp(-i \cdot \varphi_0^m(T_0)), \quad (4)$$

with M measurements $m = 0, \dots, M$. The magnitude of the resulting signal $|y_{BB}(t)|$ is shown in Figure 5.b) (red line). Finally, we shift the baseband signal to the transmission band at the measurement center frequency $f_{c,k} = \{3.5, 4.0, 4.5\}$ GHz where $k = 1, 2, 3$ is the UWB channel

$$y_k(t) = y_{BB}(t) \cdot \exp(i \cdot 2\pi \cdot f_{c,k} \cdot t). \quad (5)$$

The reconstructed received signal is shown in Figure 5.b) (blue line). In previous work [10], we assembled signals on distinct transmission bands from the same measurement environment to create a larger transmission bandwidth $B_a > B$. The DW1000 provides measurements on the transmission bands $B_{T,1}, B_{T,2}, B_{T,3}$, which are neighboring bands each with a bandwidth $B = 500$ MHz. The assembled received signal $y_a(t)$ is [10]:

$$y_a(t) = \sum_{k=1}^3 y_k(t), \text{ with bandwidth } B_a = 1.5 \text{ GHz} \quad (6)$$

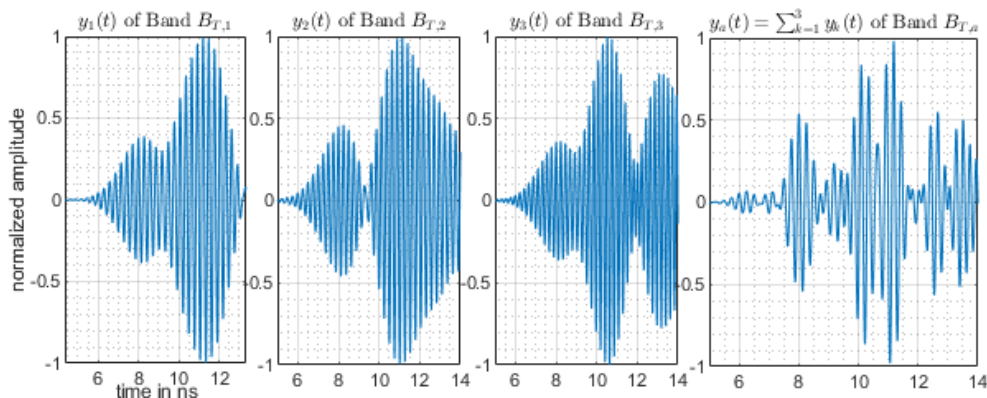


Figure 6: Measured and pre-processed UWB signals $y_1(t), y_2(t)$ and $y_3(t)$ of transmission bands $B_{T,1}, B_{T,2}, B_{T,3}$ and the assembled $y_a(t)$ of one tag position P_T .

Figure 6 shows the three processed received signals at one tag position as well as the resulting assembled received signal. We determine the assembled received signal for each tag position as an input for the peak detection algorithm depicted in the next section.

3.2. MPC Estimation and Real CIR-vector Measurements

After processing our measurements for MPC detection, we will briefly introduce our modified peak detection algorithm, which evolves based on our previous work [10].

Algorithm 3: Modified pseudo-code for MPC detection from previous work [10].

Data:
received signal $y_{It}(t) = y_a(t)$; amplitude-threshold: $a_t \in \mathbb{R}^+$;
MPC-threshold: $I_t \in \mathbb{N}$; counter: $c \leftarrow 1$;

- 1 **while** $\nexists c' : |\hat{\mathbf{a}}[c']| < a_t$ OR $c \leq I_t$ **do**
- 2 $y_{conv}(t) = y_{It}(t) * x(-t)$;
- 3 $\hat{\tau}[c] \leftarrow \arg \max_{t \in \mathbb{R}^+} (y_{conv}(t))$;
- 4 $w_c(t) = x(t - \hat{\tau}[c])$;
- 5 $\mathbf{w}_{cmb} = [w_1[kT_S]^T, \dots, w_c[kT_S]^T]^T, k \in \mathbb{N}$;
- 6 $\begin{bmatrix} \hat{\mathbf{a}}[1] \\ \vdots \\ \hat{\mathbf{a}}[c] \end{bmatrix} = [\mathbf{w}_{cmb} \cdot \mathbf{w}_{cmb}^T]^{-1} \times [\mathbf{w}_{cmb} \cdot y[kT_S]^T]$;
- 7 $c = c + 1$;
- 8 $y_{It}(t) = y_a(t) - \sum_{i=1}^c \hat{\mathbf{a}}[i] \cdot x(t - \hat{\tau}[i])$;
- 9 **end**

For MPC detection, we use the algorithm depicted in 3. We correlate the transmit signal $x(t)$ with the assembled received signal $y_a(t)$ to find the most likely position of $x(t)$ in $y_a(t)$. Afterward, we calculate the corresponding amplitudes $\hat{\mathbf{a}}$ of all determined signal echos and subtract them from the overall received signal. This is calculated iteratively until either one of the calculated signal echo amplitudes $\hat{\mathbf{a}}$ falls below a self-set amplitude-threshold a_t . We modified the code so that also the number of detectable MPCs is limited to I_t . Then the set of estimated MPCs with delay $\hat{\tau}$ and amplitude $\hat{\mathbf{a}}$ form our measured CIR $h_{meas}(t)$ as shown in (1).

In prior work, we elaborated that a larger bandwidth decreases the minimum delay difference $\Delta\tau$ between two MPCs required for successful MPC detection with the given algorithm. In our case with bandwidth $B_a = 1.5$ GHz, we determined a minimum distance of $\Delta\tau = 0.78$ ns. Furthermore, this minimum distance is used for defining the bin width for conversion of the CIR-vectors $\Delta_{bin} = \Delta\tau = 0.78$ ns. In Algorithm 1, we convert the estimated CIR $h_{meas}(t)$ to the measured CIR-vector \mathbf{h}_{meas} . An exemplary comparison for MPC detection of an assembled received signal with the modeled CIR including the resulting CIR-vectors is shown in Figure 7.

In this section, we focus on (pre-)processing of the measurement and extracting the MPC estimations from it. In the following section, we evaluate the localization system.

4. Accuracy and Ambiguity of SALOS

After introducing the single tools of SALOS, our proposed localization system, we will now evaluate the accuracy of the system. Additionally, one of the main aims of SALOS is to reduce the demand for external information to ensure unambiguity of the mapping from CIR-vector \mathbf{h}_{P_T} to position P_T . In the first part of this section, we describe our evaluation setup with our general algorithmic order. Then, we will present the results.

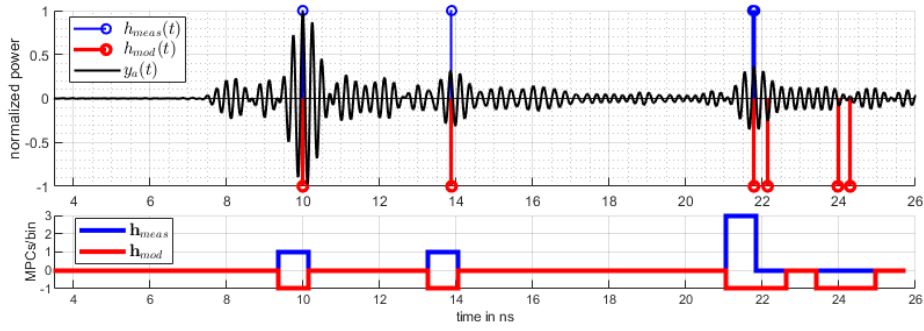


Figure 7: Example of comparison for measured h_{meas} and modeled h_{mod} for a position estimation.

4.1. Measurement Setup with Optimal Anchor Positioning

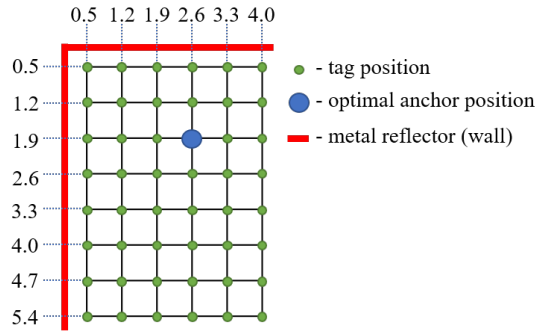


Figure 8: Grid of the evaluation setup.

For the evaluation of SALOS, a suitable test environment must be selected. In order to validate the algorithm of the system, this environment should be clearly assigned to the simulated multipath propagation. On the one hand, the success of the system evaluation depends on a small and distinct number of reflectors and therefore reflections. However, a small number of reflectors reduces the ability to characterize the paths and thus the tag positions at suboptimal places. Also, the choice of reflector material significantly affects the reflected signal energy of the echoes and thus the received signal. While perfect reflectors do not exist in all environments, this optimization enables the evaluation focus on the system itself independent from bad reflection behavior. The knowledge gained in the chosen optimal scenario is taken into account when installing the system in a more complex scenario in the future.

For performance evaluation, we choose an advantageous setup. we set up an outdoor measurement grid sketched in Figure 8. The environment includes two metal garage doors (red lines) and the ground as reflectors resulting in three reflecting surfaces for the multipath propagation. The grid consists of 48 grid points with a distance of 0.5 m to the walls and a spacing of 0.7 m

between the single points. One grid point is the position of the anchor P_A , the remaining 47 points are tag positions $\{P_T\}$. The anchor and tag are placed at a fixed height of 1.5 m.

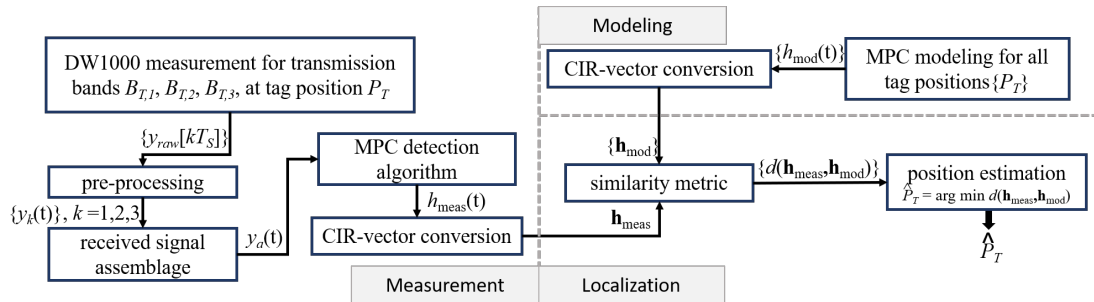


Figure 9: Block diagram of SALOS.

Figure 9 depicts the block diagram of SALOS. According to 2.1 and 2.3, we modeled the multipath propagation in this environment and determined the optimal anchor position at $P_A = [2.6, 1.9]$ m with an effective length of $l_e = 33 \cdot \Delta_{bin} = 25.74$ ns. Based on this optimal anchor position, we converted the modeled CIRs $\{h_{mod}(t)\}$ for all 47 tag positions into CIR-vectors \mathbf{h}_{mod} . The tag is placed at $\{P_T\}$. At every position, we record $M = 100$ received signals for each transmission band $B_{T,1}$, $B_{T,2}$ and $B_{T,3}$ with Qorvo’s Decawave DW1000. The radio settings of the DW1000 are found in Table 1. Each set of measurements is processed and assembled to construct $y_a(t)$ as described in Section 3.1. Afterward, we estimate the MPCs with Algorithm 3 and convert the resulting CIR estimate $h_{meas}(t)$ to the CIR-vector \mathbf{h}_{meas} . For this, we set the amplitude threshold of the MPC detection algorithm empirically to $a_t = 0.1$ of the maximum amplitude of the individual received signal.

We apply the similarity metrics of Section 2.4 to calculate the difference between one measurement CIR-vector \mathbf{h}_{meas} with the modeled CIR-vectors of all positions $\{\mathbf{h}_{mod}\}$. For position estimation, we finally compare the results of the similarity metrics among themselves. We define the minimum difference of metric results to indicate the most probable tag position \hat{P}_T :

$$\hat{P}_T = \arg \min_{\{P_T\}} d(\mathbf{h}_{meas}, \mathbf{h}_{mod}). \quad (7)$$

4.2. Evaluation of Accuracy and Ambiguity of SALOS

To evaluate the accuracy, we define two evaluation cases for position estimation. In the first case, we take the CIR-vectors of *all* 47 positions and determine the position \hat{P}_T as described above based on the similarity metric. In the second case, we perform a pre-selection for the modeled CIR-vectors before comparing them with our measured CIR-vector. The selected vectors have a similar distance to the anchor as the measurement. This selection removes improbable tag positions before estimation which is increasing the accuracy and reduces the overall processing time of SALOS. All CIR-vectors with a distance $d_0 \pm \Delta d$, where d_0 is the distance of the measurement determined by the TWR, are included in this selection. Due to the standard deviation of the TWR, we define $\Delta d = 0.2$ m.

Even though a correct position is estimated for one measurement, Eq. 7 may result in a set of positions with an identical output of the similarity metric leading to ambiguities for the position estimation. So, for both approaches, we determined the number of *correct* position estimations, as well as the number of *correct and unambiguous* position estimations.

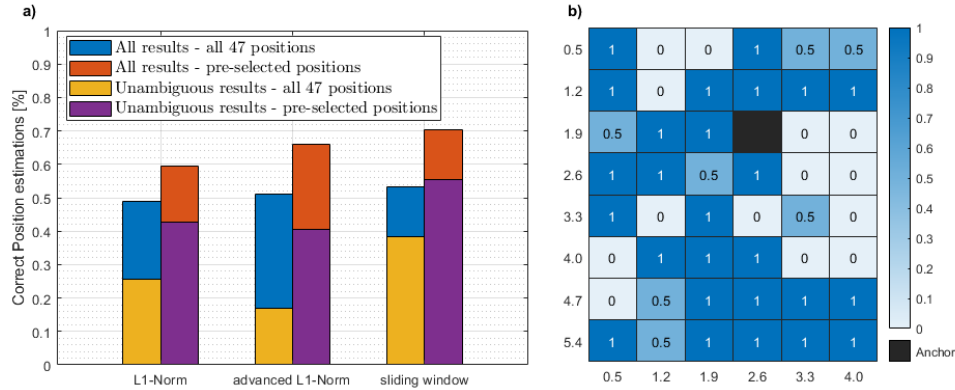


Figure 10: Results of the Evaluation

- a) Unambiguous and ambiguous correct position estimations - for all 47 positions and for pre-selected positions with similar distance $d_0 \pm \Delta d$.
b) Ambiguity of position estimations for sliding window metric with pre-selected positions.

Figure 10 a) depicts the localization results for both approaches. The accuracy of SALOS is depending on the choice of the similarity metric. For the first approach considering all modeled CIR-vectors for position estimation, the sliding window results in the highest localization accuracy of 53%. Also, our self-developed advanced ℓ_1 -norm, achieves a suitable accuracy of 51%, while the ℓ_1 -norm results in an accuracy of 49%. The second approach, that only considers a pre-selected set for position estimation increases, as expected, the accuracy of all metrics drastically. The best result is achieved with the ℓ_1 sliding window metric and an accuracy of 70%.

Measurement inaccuracies lead to a shifting of the MPCs to the CIR-vectors, even though these MPCs are detected correctly. The similarity metric needs to handle these mistakes to result in correct position estimation. While the ℓ_1 -norm is prone to these mistakes, our advanced ℓ_1 -norm performs better.

Also, the number of unambiguous position estimations is shown in Figure 10 a) for all metrics in both approaches. Here, again, the sliding window metric results in the highest number of correct unambiguous position estimations. The pre-selection approach maximizes this number with 55%. Our advanced ℓ_1 -norm performs suboptimal (16% for the first and 40% for the pre-selection approach). It needs to be improved in the future.

Figure 10 b) shows the ambiguity of single position estimations. It depicts the number of estimates for the sliding window in the pre-selection approach. The value displayed is the number of correct position estimations divided by the number of all position estimations for the exact position. E.g. $0.5 = 1/2$ results in a correct estimate, but with another incorrect estimate forming the set of estimates.

We see that on the right-hand side of the setup (without reflecting surface) as well as for positions quite close to the reflectors some positions are not estimated correctly. Positions close to the reflectors lead to reflection paths with similar path lengths to the LOS with d_0 , which increases the difficulty of the MPC detection algorithm.

Although some positions are confused, no structured regularities for the ambiguities emerge. We introduce the *assessment of ambiguity* A_{amb} to quantify the capability of similarity metrics to decrease the demand for external information. A_{amb} results from calculating the average of all (partly) correct estimate results. From Figure 10 b) follows: $A_{amb} = (26 \cdot 1 + 7 \cdot 0.5)/33 = 0.89$. Table 2 lists the position estimation accuracy as well as A_{amb} for all six given setups.

Table 2

Assessment of ambiguity A_{amb} for all metrics.

Setup	accuracy	A_{amb}
ℓ_1 -norm - all positions	49%	0.67
ℓ_1 -norm - pre-selected positions	60%	0.80
advanced ℓ_1 -norm - all positions	51%	0.61
advanced ℓ_1 -norm - pre-selected positions	66%	0.77
ℓ_1 sliding window - all positions	53%	0.85
ℓ_1 sliding window - pre-selected positions	70%	0.89

The assessment of ambiguity A_{amb} is independent of the localization accuracy. It is increased by pre-selecting positions for position estimation. For SALOS, the ℓ_1 sliding window metric maximizes A_{amb} with 0.85 and the localization accuracy of 53% for all positions and respectively to 0.89 and the localization accuracy of 70% for pre-selected positions.

5. Conclusion and Future Work

In this paper, we introduced SALOS a single anchor localization system based on COTS hardware. We combined our previous theoretical and basic results into a complete solution. For a setup of 47 grid points, we achieved 70% of correct position estimations based on our measurements in the best case. The advantage of SALOS compared to other solutions is that we modeled the environment and the expected CIRs. We solely used the measurements of the UWB signals and estimated the position based on filter and processing algorithms without the need for fingerprints or additional external information or filters.

In the future, we will implement SALOS as online real live localization system and extend the solution to adjust for a dynamic multipath environment. For this, we will choose a more complex indoor environment including also suboptimal reflectors. Based on the setup and the results of the optimally chosen measurement setup of this work, we will make a statement about the position accuracy of the system to compare it with other localization approaches, like UWB systems with two and more anchors.

Acknowledgements

This publication results from research of Center of Excellence CoSA at the Technische Hochschule Lübeck and is funded by the Federal Ministry of Economic Affairs and Energy of the Federal Republic of Germany (Id 03SX467B, Project EXTENSE, Project Management Agency: Jülich PTJ). Horst Hellbrück is an adjunct professor at the Institute of Telematics of University of Lübeck.

References

- [1] S. Leugner, H. Hellbrück, Lessons learned: Indoor Ultra-Wideband localization systems for an industrial IoT application, Technical Report, Technische Universität Braunschweig, Braunschweig, 2018. doi:10.24355/dbbs.084-201807191346-0.
- [2] B. Figueira, B. Gonçalves, H. Folgado, N. Masiulis, J. Calleja-González, J. Sampaio, Accuracy of a basketball indoor tracking system based on standard bluetooth low energy channels (nbn23®), *Sensors* 18 (2018) 1940.
- [3] M. Qian, K. Zhao, A. Seneviratne, B. Li, Performance analysis of ble 5.1 new feature angle of arrival for relative positioning, *The International Archives of Photogrammetry, Remote Sensing and Spatial Information Sciences* 46 (2022) 155–161.
- [4] B. Großwindhager, M. Rath, J. Kulmer, M. S. Bakr, C. A. Boano, K. Witrissal, K. Römer, SALMA: UWB-based single-anchor localization system using multipath assistance, in: *Proceedings of the 16th ACM Conference on Embedded Networked Sensor Systems*, 2018.
- [5] T. Wang, H. Zhao, Y. Shen, An efficient single-anchor localization method using ultra-wide bandwidth systems, *Applied Sciences* 10 (2019) 57.
- [6] Y. Cao, C. Yang, R. Li, A. Knoll, G. Beltrame, Accurate position tracking with a single uwb anchor, in: *2020 IEEE international conference on robotics and automation (ICRA)*, IEEE, 2020, pp. 2344–2350.
- [7] P. Meissner, E. Leitinger, M. Fröhle, K. Witrissal, Accurate and robust indoor localization systems using ultra-wideband signals, *arXiv preprint arXiv:1304.7928* (2013).
- [8] Q. Miao, B. Huang, On the optimal anchor placement in single-hop sensor localization, *Wireless Networks* 24 (2018) 1609–1620.
- [9] S. O. Schmidt, M. Cimdins, H. Hellbrück, On the effective length of channel impulse responses in uwb single anchor localization, in: *2019 International Conference on Localization and GNSS (ICL-GNSS)*, 2019, pp. 1–6. doi:10.1109/ICL-GNSS.2019.8752644.
- [10] S. O. Schmidt, H. Hellbrück, Detection and identification of multipath interference with adaption of transmission band for uwb transceiver systems, in: *2021 International Conference on Indoor Positioning and Indoor Navigation (IPIN)*, 2021, pp. 1–16. <http://www.ceur-ws.org/Vol-3097/paper4.pdf>.
- [11] APS013 Application Note - The implementation of two-way-ranging with the DW1000, Technical Report, Qorvo Denmark ApS, v2.3.
- [12] DW1000 User Manual, Technical Report, Qorvo Denmark ApS, v2.11.
- [13] M. Cimdins, S. O. Schmidt, H. Hellbrück, MAMPI-UWB—Multipath-Assisted Device-Free Localization with Magnitude and Phase Information with UWB Transceivers, *Sensors* 20 (2020) 7090.